Vortex Pinning in High-T_c Superconductors

A thesis submitted in partial fulfillment of the requirement
for the degree of Bachelor of Science
Physics from the College of William and Mary in Virginia,

by

Abigail C. Shockley

Accepted for: BS in Physics

Advisor: W. J. Kossler

Gina Hoatson

Williamsburg, Virginia
May 2007

Abstract

We have studied vortex pinning in High-Tc superconductors by examining experimental μ-SR data collected at TRIUMF. Using the theoretical model for vortex pinning proposed by E.H. Brandt, we have analyzed the second moment of the magnetic field for the superconductor BSCCO. We used four different theoretical models for the behavior of the penetration depth in a superconductor to determine whether BSCCO could be considered d-wave or s-wave.

Acknowledgements

I would first like to thank my research advisor, Jack Kossler, for not only providing me guidance on this project but for providing support with my personal issues as well. On that note, I would also like to thank Marc Sher, Jeff Nelson, Jan Chaloupka, and Gina Hoatson for providing a similar form of guidance. The physics department has miraculously helped me keep myself together and finish out this year. I don't know that I can fully express my gratitude in words.

Contents

1 Introduction

Historically, Kammerlingh Onnes discovered the first superconductor (mercury) in 1911. Superconductors have the unusual property that under a certain temperature they have zero electrical resistance [1]. In 1956, Cooper proposed that two electons interacting with each other in a Fermi sea background form bound states for an arbitrarily weak attractive force. The resulting bound electron pairs are called Cooper pairs and become the carriers of the super-current [2]. In general, there are two main types of superconductors: Type I and Type II. High-T_c superconductors are classified as Type II.

1.1 London Equation

The London equation allows us to determine the magnetic field distribution of a superconductor explicitly [1]. This field distribution depends primarily upon the penetration depth which is one of the characteristic parameters of a superconductor.

We will start by considering one of Maxwell's equations, which in Gaussian units is:

$$\nabla \times \mathbf{B} = \frac{4\pi}{c}\mathbf{j} \tag{1}$$

To find a second relation for the current density $\mathbf{j}$, consider an electron with charge e moving at velocity $\mathbf{v}$ at time 0. The current density can then be expressed as

$$\mathbf{j} = n_s e\mathbf{v} \tag{2}$$

where n_s is the number of superconducting electrons. Taking the time derivative of Eq 2,

$$\frac{d\mathbf{j}}{dt} = n_s e\mathbf{a} = \frac{n_s e^2}{m}\mathbf{E} \tag{3}$$

where **a** is the acceleration due to an electric field **E** and m is the mass of an electron. From another one of Maxwell's equations, the electric field is related to the magnetic field:

$$\nabla \times \mathbf{E} = -\frac{1}{c}\frac{d\mathbf{B}}{dt} \tag{4}$$

Inserting Eq 4 into Eq 3, integreating and arbitrarily setting the integration constant to zero, we have

$$\nabla \times \mathbf{j} = -\frac{n_s e^2}{mc}\mathbf{B} \quad or \quad \mathbf{j} = -k\mathbf{A} \tag{5}$$

Returning to Eq 1, we want a relation involving the curl of j.

$$\begin{aligned} \frac{4\pi}{c}\nabla \times \mathbf{j} &= \nabla \times (\nabla \times \mathbf{B}) \\ &= \nabla(\nabla \cdot \mathbf{B}) - \nabla^2\mathbf{B} \end{aligned}$$

Using Maxwell's equation $\nabla \cdot \mathbf{B} = 0$ and Eq 5, we have

$$\nabla^2\mathbf{B} - \frac{4\pi n e^2}{mc^2}\mathbf{B} = 0 \tag{6}$$

which is known equivalently with Eq 5 as the London equation. This equation was first proposed by F. and H. London [1].

1.2 Penetration Depth

The penetration depth is defined as

$$\lambda_L = \left(\frac{mc^2}{4\pi n_s e^2}\right)^{\frac{1}{2}} \tag{7}$$

where n_s is the number of superconducting electrons so that Eq 6 reads

$$\nabla^2\mathbf{B} - \frac{1}{\lambda_L^2}\mathbf{B} = 0 \tag{8}$$

In a plane geometry situation, the field in a superconductor falls off as $H_0 e^{-x/\lambda_L}$. This justifies the description of λ_L as a penetration depth.

1.3 Coherence Length

Degennes [1] discusses the coherence length which is roughly the size of the cooper pair. Our derivation of the London equation assumes a slow variation in space of the supercurrent **j**. In order for the London equation to be valid, we must define what is meant by slow. The velocities of two electrons are correlated if the distance between them is smaller than a certain range. For pure metals, the correlation length is called ξ_0. Our derivation applies when the supercurrent has a negligible variation over distances $\sim \xi_0$. To estimate ξ_0 we notice that the important domain in momentum space is defined by

$$E_F - \Delta < \frac{p^2}{2m} < E_F + \Delta \tag{9}$$

where E_F is the Fermi level and Δ is the energy gap. The gap is related to the transition temperature by $2\Delta = 3.5 k_B T_0$. Considering a Fermi sphere, the thickness of the shell is defined by Eq 9 as $\delta p \cong \frac{2\Delta}{v_F}$. From the uncertainty principle, the minimum spatial extent is $\delta x \sim \frac{\hbar}{\delta p}$. We can then take

$$\xi_0 = \frac{\hbar v_F}{\pi \Delta} \tag{10}$$

where the factor $\frac{1}{\pi}$ is arbitrary. The length ξ_0 in Eq 10 is called the coherence length of a superconductor. [1]

1.4 Type II Superconductor

For transition metals and intermetallic compounds, the effective mass is very large, λ_L is large ($\cong 2700\dot{A}$) and the Fermi velocity is small ($\cong 10^6 cm/sec$). For our purposes,

we are considering compounds with a relatively high transition temperature ($\cong 90K$). The gap Δ is roughly proportional to the transition temperature and is therefore larger. For all these reasons, ξ_0 is very small ($\cong 30\dot{A}$) for high T_c materials. For this class of materials, Eq 9 is applicable in weak fields. These materials are called Type II or London superconductors. [1]

1.5 Empirical Model

The simplest form of the temperature dependence of the penetration depth is given by

$$\left(\frac{\lambda}{\lambda_0}\right)^2 = \frac{1}{1-(\frac{T}{T_c})^\gamma} \tag{11}$$

where γ is an exponent. A phenomenological description of the penetration depth may be achieved with $\gamma = 2.0$ [3]. This simple model is often referred to as the Empirical Model.

1.6 2-Fluid Model

For the developement of the 2-Fluid Model, we will examine the magnetic properties of a superconducting sample. For a very small sample, we must take the average value of the magnetic field. Considering a plate of thickness 2a [4],

$$\bar{B} = \frac{1}{a}\int_0^a H dx = H_0\left(1 - \frac{2\gamma a^2}{3\lambda^2}\right) \tag{12}$$

The magnetic susceptibility κ for a sample is then

$$\kappa = \frac{\bar{B} - H_0}{4\pi H_0} = -\frac{\gamma a^2}{6\pi\lambda^2} \tag{13}$$

where γ is a constant depending on the theory of penetration and the geometry of the sample. Or

$$\frac{\kappa}{\kappa_0} = \frac{\alpha a^2}{\lambda^2} \tag{14}$$

where α is a constant whose value depends on whether we are considering a plate, a wire or a sphere. Since γ is an unspecified parameter, there is little point in considering the full calculation of $\frac{\kappa}{\kappa_0}$.

Considering the normalized susceptibility over an assembly of spheres, we have

$$\frac{\kappa}{\kappa_0} = \frac{\alpha a'^2}{\lambda^2} \tag{15}$$

where a'$^2 = \bar{a^5}/\bar{a^3}$ provided that a $\ll \lambda$ for all spheres. Looking at $\frac{\kappa}{\kappa_0}$ as a function of temperature, we find that the variation can be due only to a variation of λ with temperature. Since a' is only known to an order of magnitude, we may only consider relative values of λ. Experimental data is consistent with the law

$$\left(\frac{\lambda}{\lambda_0}\right)^2 = \frac{1}{1-(\frac{T}{T_c})^4} \tag{16}$$

which is commonly referred to as the 2-Fluid Model. [4]

1.7 BCS Model

Degennes [1] discusses the derivation of the BCS model. We first define a wave function such that

$$\tilde{\phi} = c\Pi_k(1 + g_k a^+_{k\uparrow} a^+_{-k\downarrow})\phi_0 \tag{17}$$

where the product extends over all plane wave states, k, c is a normalization constant, and u_k and v_k are real. The operator $a^+_{k\alpha}$ creates an electron in the state ($\mathbf{k}\alpha$) when operating on the state described by ϕ_0. By incorporating the factor c into the product, we obtain

$$\tilde{\phi} = \Pi_k (u_k + v_k a^+_{k\uparrow} a^+_{-k\downarrow}) \phi_0 \tag{18}$$

with

$$\frac{v_k}{u_k} = g_k \qquad u_k^2 + v_k^2 = 1 \tag{19}$$

Letting $\mathcal{H}$ be the Hamiltonian of the interacting electron system, we can use the variational principle to minimize the expression

$$< \tilde{\phi} \mid \mathcal{H} \mid \tilde{\phi} > - E_F < \tilde{\phi} \mid N \mid \tilde{\phi} > \tag{20}$$

where N is the average number of particles and E_F, a Lagrange multiplier, is the Fermi energy.

In order to minimize $< \tilde{\phi} \mid \mathcal{H} \mid \tilde{\phi} >$ taking account of the relation $u_k^2 + v_k^2 = 1$, we set

$$u_l = \sin\theta_l \qquad v_l = \cos\theta_l \tag{21}$$

$$< \tilde{\phi} \mid \mathcal{H} \mid \tilde{\phi} >= 2 \sum_k \xi_k \cos^2\theta_k + \frac{1}{4} \sum_{kl} \sin 2\theta_k \sin 2\theta_l V_{kl} \tag{22}$$

where V_{kl} is a term that represents the interaction energy for the transition of a pair of electrons from the state ($\mathbf{k}\uparrow$,-$\mathbf{k}\downarrow$) to the state ($\mathbf{l}\uparrow$,-$\mathbf{l}\downarrow$) and $\xi_k = \frac{\hbar^2 k^2}{2m} - E_F$. The minimization equations are

$$0 = \frac{\partial}{\partial \theta_k} < \tilde{\phi} \mid \mathcal{H} \mid \tilde{\phi} >= -2\xi_k \sin 2\theta_k + \sum_l \cos 2\theta_k \sin 2\theta_l V_{kl} \tag{23}$$

or

$$\xi_k \tan 2\theta_k = \frac{1}{2} \sum_l V_{kl} \sin 2\theta_l \tag{24}$$

We define

$$\Delta_k = -\sum_l V_{kl} u_l v_l \tag{25}$$

$$\epsilon_l = \sqrt{(\xi_l^2 + \Delta_l^2)} \tag{26}$$

and we find

$$\tan 2\theta_l = -\frac{\Delta_l}{\xi_l} \tag{27}$$

$$2u_l v_l = \sin 2\theta_l = \frac{-\Delta_l}{\xi_l} \tag{28}$$

$$-u_k^2 + v_k^2 = \cos 2\theta_k = -\frac{\xi_k}{\epsilon_k} \tag{29}$$

Inserting the value of $u_l v_l$ into Eq 25, we obtain an expression for Δ

$$\Delta_k = -\sum_l V_{kl} \frac{\Delta_l}{2(\xi_l^2 + \Delta_l^2)^{\frac{1}{2}}} \tag{30}$$

The BCS interaction is chosen as

$$\begin{aligned} V_{kl} &= -V \qquad if \ \ |\, \xi_k \,|, |\, \xi_l \,| \leq \hbar\omega_D \\ &= 0 \qquad otherwise \end{aligned}$$

where ω_D is a frequency. Then we have

$$\begin{aligned} \Delta_k &= 0 \qquad for \ \ |\, \xi_k \,| > \hbar\omega_D \\ \Delta_k &= \Delta \qquad (independent\ of\ k)\ for \ \ |\, \xi_k \,| < \hbar\omega_D \end{aligned}$$

We can now write

$$\Delta = N(0)V \int_{-\hbar\omega_D}^{\hbar\omega_D} \Delta \frac{d\xi}{2(\Delta^2 + \xi^2)^{\frac{1}{2}}} \tag{31}$$

where N(0) is the number of electrons at the Fermi level. This can be solved for Δ.[1] At finite temperatures, it can be shown [5] that Eq 31 can be rewritten as

$$\frac{1}{N(0)V} = \int_0^{\hbar\omega_D} \frac{\tanh \frac{1}{2}\beta(\xi^2 + \Delta^2)^{\frac{1}{2}}}{(\xi^2 + \Delta^2)^{\frac{1}{2}}} d\xi \tag{32}$$

which yields a $\Delta(T)$.

In Fourier space, Eq 5 generalizes to

$$\mathbf{j}(\mathbf{q}) = \frac{-c}{4\pi}\mathbf{K}(\mathbf{q})\mathbf{A}(\mathbf{q}) \tag{33}$$

for an isotropic system.

From this, one can show that

$$\mathbf{K}(0,T) = \lambda_L^{-2}(T) = \lambda_L^{-2}(0)\left[1 - 2\int_\Delta^\infty \left(-\frac{\partial f}{\partial E}\right) \frac{E}{(E^2 - \Delta^2)^{\frac{1}{2}}} dE\right] \tag{34}$$

1.8 D-wave Model

A generalization of the BCS model for the situation in which the interaction energy has D-wave symmetry has been introduced by Anderson and Morel [6]. Using this model, Amin et. al. [7] generalized the BCS connection between the vector potentila and current of Eq 33 to

$$\mathbf{j}_k = -\frac{c}{4\pi}\hat{\mathbf{Q}}(k)\mathbf{A}_k \tag{35}$$

where $\hat{\mathbf{Q}}$(k) is the electromagnetic response tensor. From Amin [7], one finds that in solving the Gorkov equations generalized for an anisotropic gap the kernel of $\hat{\mathbf{Q}}$ is

$$Q_{ij}(\mathbf{k}) = \frac{4\pi T}{\lambda_0^2} \sum_{n>0} < \frac{\Delta_{\hat{p}}^2 \hat{v}_{F_i} \hat{v}_{F_j}}{(\omega_n^2 + \Delta_{\hat{p}}^2)^{\frac{1}{2}}(\omega_n^2 + \Delta_{\hat{p}}^2 + \gamma_k^2)} > \tag{36}$$

where $\gamma_k = v_F \cdot \frac{k}{2}$, λ_0 is the London penetration depth, $\omega_n = \pi T(2n-1)$ are the Matsubara frequencies and the angular bracket means Fermi surface averaging. For the purposes of this paper, we will not go into further detail on the latter two subjects.

We write the London equation solely in terms of magnetic field:

$$\mathbf{B_k} - \mathbf{k} \times [\hat{\mathbf{Q}}^{-1}(\mathbf{k})(\mathbf{k} \times \mathbf{B_k})] = 0 \tag{37}$$

To account for the phase winding around the vortex cores, we insert a source term F($\mathbf{k}$)= $e^{-\xi_0^2 k^2/2}$ on the right hand side of Eq 37.

We define λ_{eff} by

$$\lambda_{eff}^{-4} = \lambda_0^{-4}(\frac{\delta\bar{B}^2}{\delta\bar{B}_0^2}) \tag{38}$$

where $\delta\bar{B}^2$ is the second moment of the field distribution in the vortex lattice and $\delta\bar{B}_0^2$ is the same quantity for the magnetic field B_0(r) obtained by solving the London model for a triangular lattice with the same $\bar{B}$ and λ_0. Using Eq 37 and 38, we find

$$\lambda_{eff}^{-4} = C \sum_{k \neq 0} \frac{e^{-\xi_0^2 k^2}}{(1 + \mathcal{L}_{ij} k_i k_j)^2} \approx C \sum_{k \neq 0} \frac{e^{-\xi_0^2}}{(\mathcal{L}_{ij} k_i k_j)^2} \tag{39}$$

where $\mathbf{k}$ are the reciprocal lattice wave vectors and

$$\mathcal{L}_{ij}(\mathbf{k}) = \frac{Q_{ij}(\mathbf{k})}{det\hat{\mathbf{Q}}(\mathbf{k})} \quad , \quad C^{-1} = \sum_{k \neq 0} \frac{e^{-\xi_0^2 k^2}}{k^4}. \tag{40}$$

1.9 Pinning Model for Vortex Line Behavior

In a highly anisotropic superconductor, an individual vortex can be represented as a stack of two-dimensional vortices which create a Vortex-Line Lattice (VLL). In the lowest energy configuration in the absence of pinning and thermal vibration, the vortex-line will be straight. Pinning and thermal vibrations produce displacement of the vortices. Two types of vortex displacement are considered: the deviation

of the individual vortex from the smooth vortex-line, u_p, and the deviation of the smooth vortex-line from the VLL, u_l. [8, 9]. These displacements are represented schematically in Fig. 1.

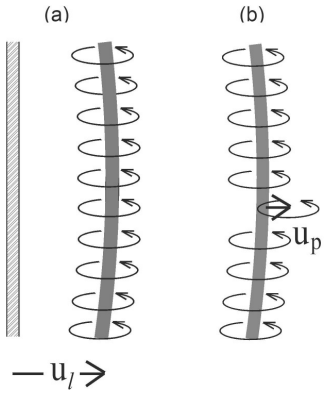

Figure 1: Fig. 1. Drawings to illustrate an anisotropic vortex decomposed into a stack of two-dimensional point vortices. (a) The local smooth vortex-line is displaced by a distance u_l from a lattice site that is represented by the bar to the left. (b) u_p is the distance an individual point vortex is displaced from the local smooth line.

Using the result obtained by Fiory [9] and Brandt [10], displacement of type u_l creates a deformation of the VLL which changes the internal potential energy. The pinning potential energy, U_P, that induces the displacement will be proportional to u_l^2. An empirical formula can therefore use a basic relationship

$$U_P(u_l) = \eta u_l^2 \tag{41}$$

where η is a parameter that models the pinning potential experienced by a given vortex.

For weak pinning, thermal fluctuations tend to depin the vortex at high temperature (i.e., $u_l \to 0$). This is modeled by a thermal activation formula (analogous to thermally activated flux creep) for the pinning displacement:

$$u_l^2 = u_{l0}^2[1 - exp(-U_P(u_l)/k_bT)] \tag{42}$$

where u_{l0} is the pinning displacement at zero temperature. Combining Eqs. 41 and 42 and substituting dimensionless variables, $y = u_l^2/u_{l0}^2$ and $x = k_bT/\eta u_{l0}^2$, one obtains the transcendental equation:

$$y = 1 - exp(-y/x) \tag{43}$$

Averaging Eq. 43 over all space and solving numerically, the following result is obtained:

$$\bar{y}(x) = exp[-1.4503x - 0.38627x^2] \tag{44}$$

The mean square displacement of the vortices from the ideal lattice positions is then

$$< u_l^2 >= u_{l0}^2 \bar{y}[k_bT/E_P(T)] \tag{45}$$

where the quantity $E_P(T) \equiv \eta u_{l0}^2$ represents the mean pinning activation energy.

Local pinning forces and thermal excitation create displacements of type u_p. Two parameters are introduced to model these contributions to the mean square displacement, $< u_p^2 >$. The effect of pinning is modeled by a field-dependent mean variance u_{p1}^2 taken to be a temperature-independent parameter for simplicity. Thermal fluctuations, which in general are transverse waves along the vortex-lines, increase the line tension and entail a cost in energy. Displacement energy, which scales with u_p^2, is supplied by the thermal energy, k_bT, and thus is modeled by including a term in $< u_p^2 >$ that is proportional to temperature. Combining the two contributions in quadrature yields the following expression for the total variance in u_p:

$$< u_p^2 >= u_{p1}^2(H) + (T/T_c)u_{p2}^2(H) \tag{46}$$

1.10 Second Moment Model

One of the most important characteristics of a superconductor, the root second moment describes the variance in the local magnetic field. Displacements of the local vortex sites change the form of the local magnetic field distribution which changes the variance in the local magnetic field [9]. For a regular triangular lattice and in the London approximation [9], the root second moment is given by

$$\sigma_0 = 0.0609\phi_o/\lambda_{ab}^2 \tag{47}$$

where λ_{ab} is the penetration depth in the a-b plane. Fluctuations of type u_l tend to increase the value of the second moment whereas fluctuations of type u_p tend to decrease the value of the root second moment. The combined effect of mean random displacements determined by the variances $< u_l^2 > and < u_p^2 >$ on the second moment is calculated using the results obtained by Brandt [10]

$$\sigma^2 \approx \sigma_0^2[exp(-26.3u^2/a^2 + 24.8(< u_l^2 > /a^2)ln(\tilde{\kappa})] \tag{48}$$

where a is the vortex lattice parameter, $u^2 =< u_l^2 > + < u_p^2 >$, and $\tilde{\kappa}^2 = (< u_l^2 > +2\lambda_{ab}^2)/(u^2 + 4\xi_{ab}^2)$ where ξ_{ab} is the coherence length in the a-b plane.

1.11 Penetration Depth and the Theoretical Models

In the four theoretical models mentioned above, the root second moment of the field relates to $\lambda(0)^2/\lambda(T)^2$.

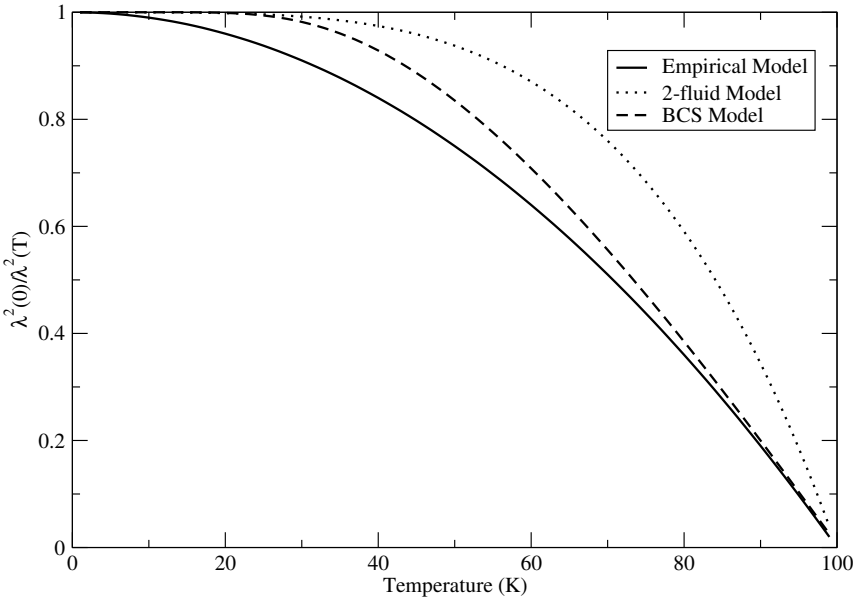

Figure 2: $\lambda(0)^2/\lambda(T)^2$ are displayed as a function of temperature for the Empirical, 2-Fluid, and BCS models.

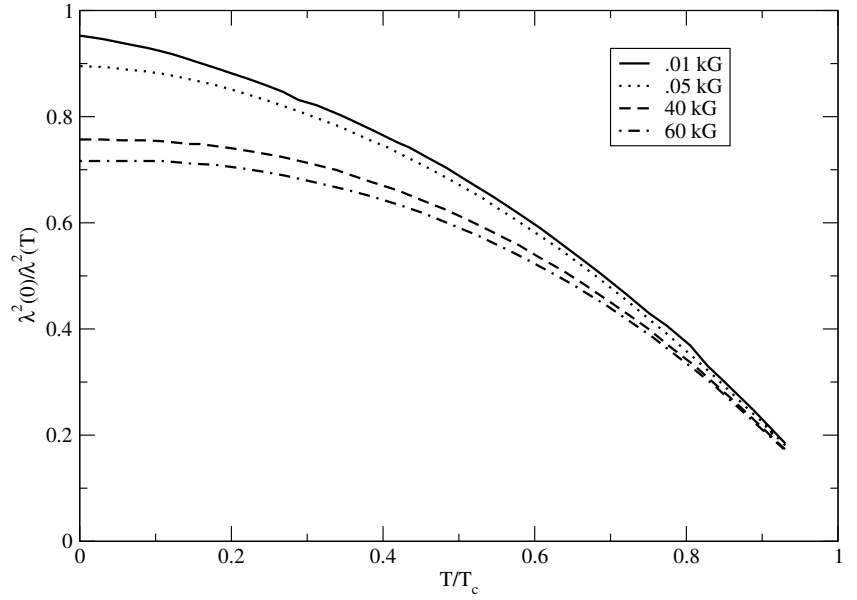

Figure 3: $\lambda(0)^2/\lambda(T)^2$ are displayed as a function of the normalized temperature for the D-wave model. Note that for the d-wave model, these values also depend on the magnetic field.

2 Experiment

Muon spin rotation (μ-SR) experiments were conducted at the TRIUMF cyclotron facility in Vancouver, British Columbia, Canada using the Belle (high-field) spectrometer.

2.1 μ-SR Technique

In μ-SR, positive muons can be used as a probe of magnetism. They are produced with perfect polarization. The muons are stopped in the sample, where they decay with each emitting a positron preferentially along the final spin-polarization direction [8]. When the incident muon enters the sample, a clock is started and stopped upon detection of the decay positron. By this method, the time evolution of positive muons' spins are measured one at a time to yield an ensemble average. This ensemble average is used to detemine, e.g., the variance in the local magnetic field of the BSCCO sample. Fig. 4 is an example of an ensemble average taken for the superconductor BSCCO. For this experimental setup, there are four detectors at the top, bottom, left and right of the sample.

2.2 Heterodyne Technique

For high fields, the muon precision is very rapid making comparison between fitting functions and data difficult. To circumvent this problem, a heterodyning technique is used to produce oscillating data of much lower frequencies. The most common use of heterodyning is with radio frequencies. When a frequency is heterodyned, a new frequency is created by mixing two or more signals. This particular technique can convert the rapidly oscillating μ-SR data into a slower oscillating format which can be more easily analyzed.

Typically, precession has a distribution of frequencies clustered near $\omega = \gamma_\mu B$ or

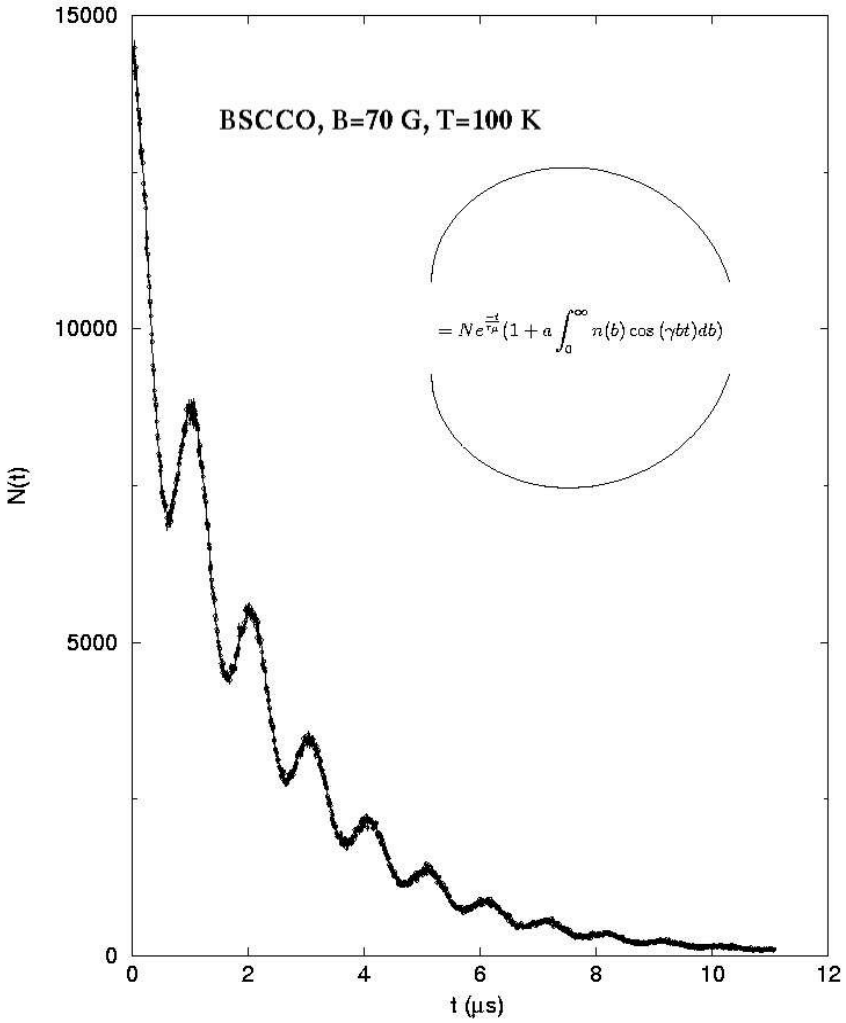

Figure 4: A μ-SR graph showing the depolarization rate of the muon decay. Presuming the magnetic field is static, the depolarization is described by $Ne^{\frac{-t}{\tau_\mu}}(1 + a\int_0^\infty n(b)\cos(\gamma bt)db)$ where n(b) is the probability distribution of the magnetic field.

$f = \frac{\gamma_\mu}{2\pi} B$ where B is the average field.To determine this average frequency which we will call the natural frequency, the μ-SR data can be Fourier transformed. Generally, the natural frequency will be

$$10 \times the applied field measured in tesla \times the Larmor frequency of the muon \quad (49)$$

To find the actual natural frequency, the range of the Fourier transform is set to 500 Mrad/s above and below the estimated natural frequency. The actual natural frequency is where the Fourier transform has an asymptote. The range can be reset until the ideal precision is reached for the actual natural frequency which is on the order of magnitude of 10^0. Fig. 5 shows a spectrum that has been Fourier transformed.

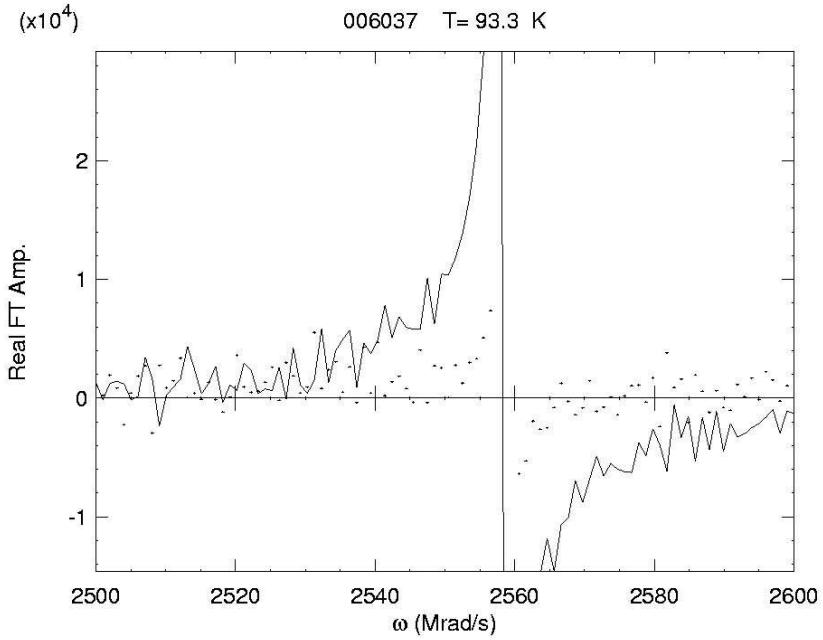

Figure 5: The Fourier Transform for an applied field of 3T. The peak for the natural frequency occurs at 2560 Mrad/s.

In order to analyze the data, the heterodyne must produce a large amount of oscillations for higher temperatures. If the heterodyne frequency is within 5 Mrad/s of the natural frequency, then approximately two to three oscillations are produced

for the high temperatures. At the lower temperatures, the field distribution is much broader so that the ensemble average has fewer oscillations. If the heterodyne frequency is chosen to be more than 20 Mrad/s over the natural frequency, the function may appear to be zero because many channels are binned together at these low temperatures. By analyzing the data with various heterodyne frequencies within this range, we found that the actual heterodyne frequency negligbly affected the results obtained. In general, we chose a heterodyne frequency that was 10 Mrad/s less than the natural frequency. Fig. 6 and Fig. 7 are examples of a bad and a good heterodyne, respectively.

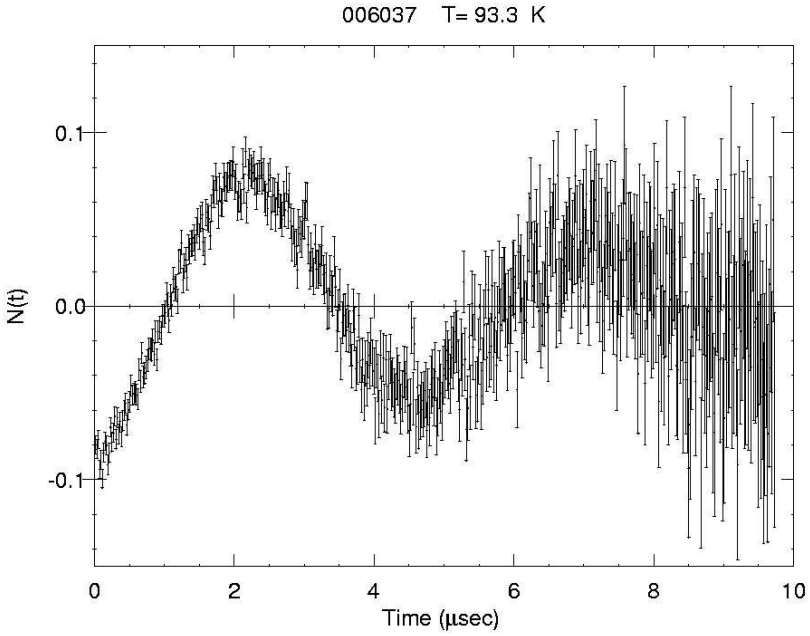

Figure 6: Data at an applied field of 3T that has been heterodyned with a frequency of 2558 Mrad/s. This heterodyne frequency is too close to the natural frequency; the curve has too few oscillations to be analyzed.

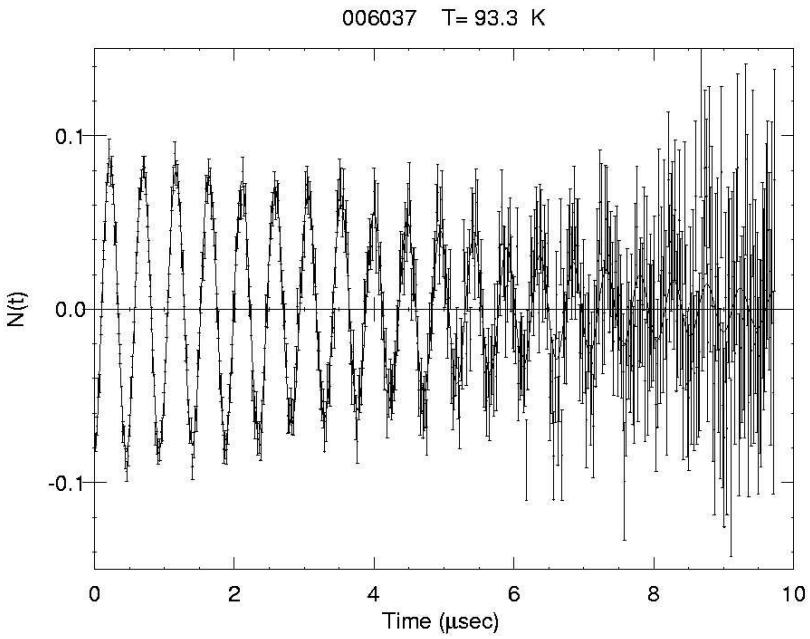

Figure 7: Data at an applied field of 3T that has been heterodyned with a frequency of 2550 Mrad/s. This is an example of what an appropriate heterodyne frequency will produce.

2.3 Fitting the Data

The program trix06 was written to analyze data from the TRIUMF facility [11].

2.3.1 Function 34

For the data collected from the Belle detector, function 34 has been used for each of four detectors:

$$y = \sum a_1...a_4 e^{\frac{-(\omega-\omega_0)^2}{2\omega_x^2}} \cos(\omega t + \phi(i)) + a_{12}...a_{15} e^{\frac{-a_{16}^2 t^2}{2}} \cos(\omega_0 t + \phi) \qquad (50)$$

where $a_1...a_4$ are the amplitudes of a second component, a_5 is ω_0, a_6 is ω_{ave}, a_7 is ω_d, $a_8...a_{11}$ are phases, and $a_{12}...a_{15}$ are 2nd and σ^2. This function fits the data to a back-to-back heterodyned Gaussian-Gaussian.

2.3.2 Function 35

Function 35 was also used for each of the four detectors:

$$y = a_1...a_4(a_5 t(b + delb = a_6 + a_{17}, xi = a_{18} xlab = a_8, t, phi = a_{11} - a_{14}) \tag{51}$$

$$+ (1 - a_5)\cos(gma_9 t + a_{11} - a_{14})e^{-(a_{10}t)^2/2} + a_{15}e^{-a_{16}t}) \tag{52}$$

where $a_1...a_4$ are the amplitudes of a second component, a_5 is the fraction of superconducting electrons, a_6 is the magnetic field in Gauss, a_7 is the smearing sigma, a_8 is the penetration depth, a_9 is the background magnetic field, a_{10} is the width of the background signal, $a_{11}...a_{14}$ are phases, a_{15} and a_{16} are the tails of the graph, a_{17} is the shift of the precession rate, and a_{18} is the coherence length. This function fits the data to a London like field distribution with a core cutoff as described by Yaouanc et. al. [12].

2.3.3 Which function to use?

To determine which function to use, we examined the root second moments produced from each function shown in Figs 8, 9, 10, 11, and 12. Function 34 produces more consistent results across the various fields. For the results, we fit the data from the Belle detectors with Function 34. The systematic difference occurs because Function 35 does not go to zero as rapidly for large separations from the peak as the Gaussians in Function 34. From Fig 9, we see that the asymmetric tail is more prominent below 40K.

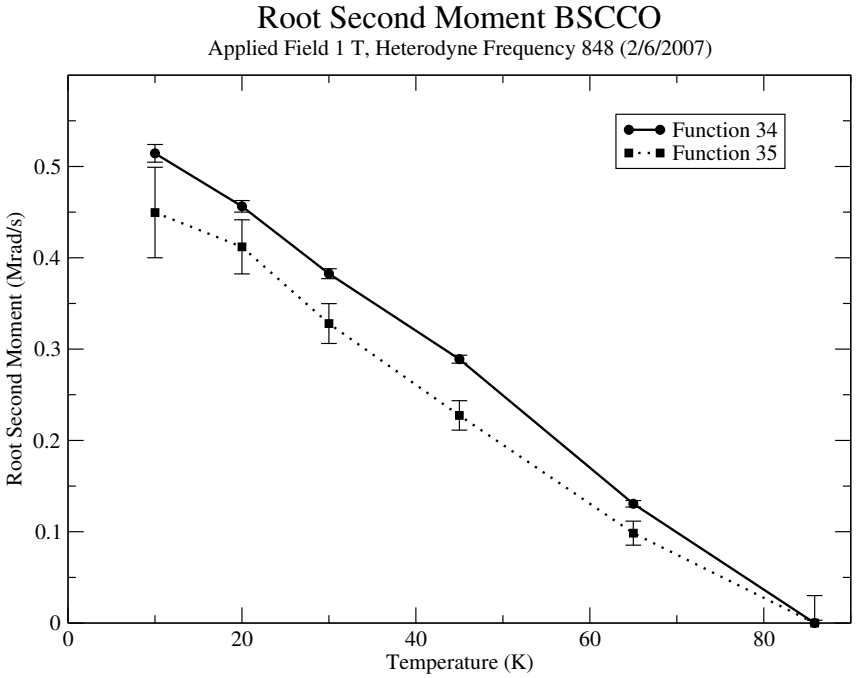

Figure 8: The root second moments produced from function 34 and 35 with an applied field of 1T.

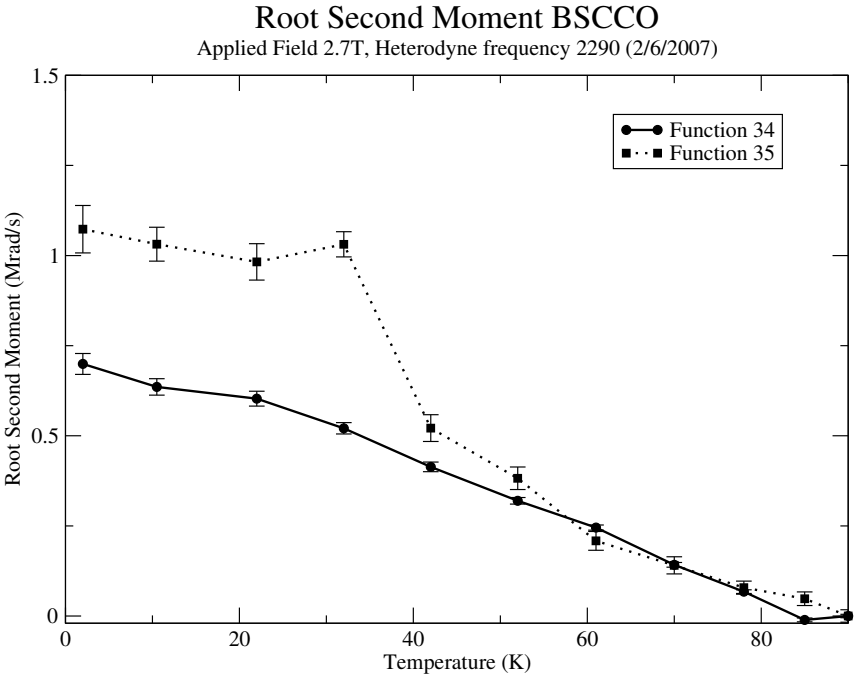

Figure 9: The root second moments produced from function 34 and 35 with an applied field of 2.7T.

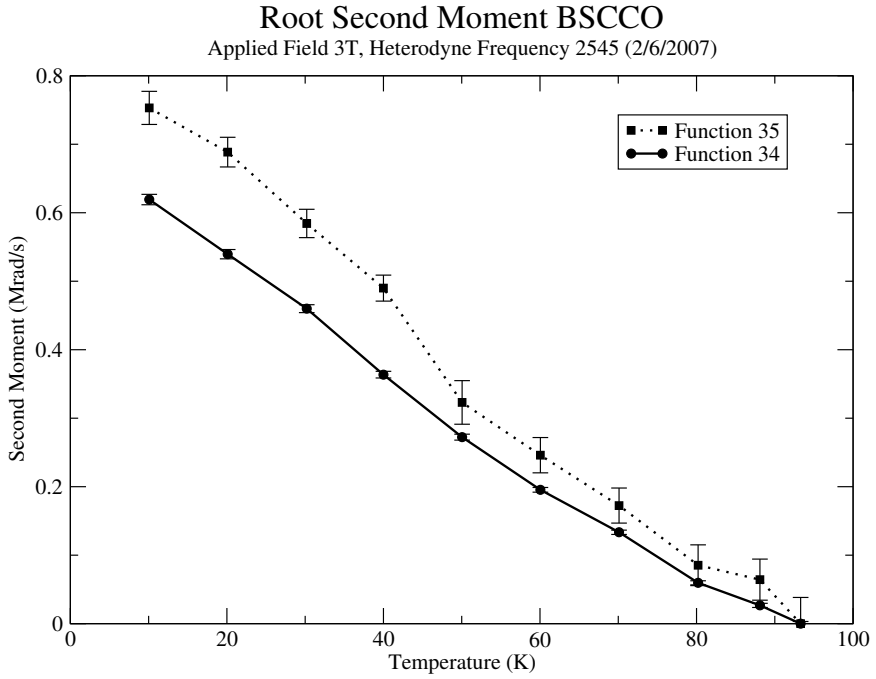

Figure 10: The root second moments produced from function 34 and 35 with an applied field of 3T.

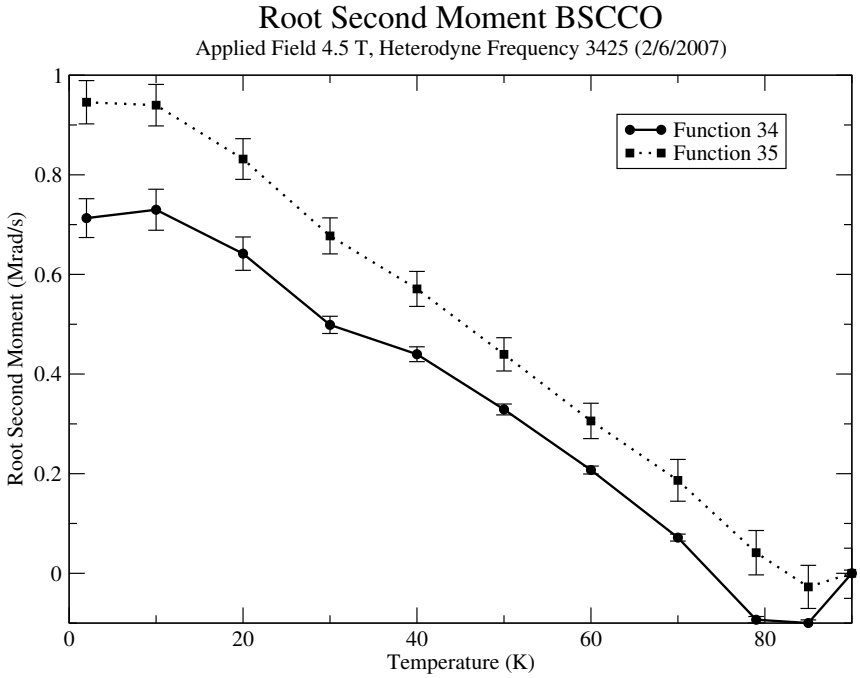

Figure 11: The root second moments produced from function 34 and 35 with an applied field of 4.5T.

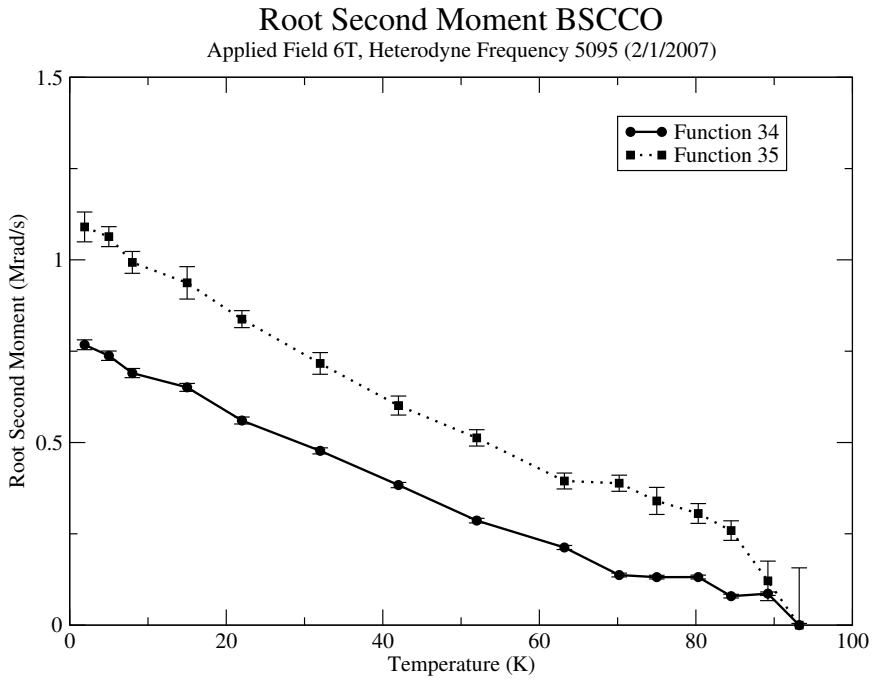

Figure 12: The root second moments produced from function 34 and 35 with an applied field of 6T.

3 Results

Using Brandt's model for the root second moment, the data from TRIUMF which was fitted with function 34 can be analyzed. Parameter a_6, ω_{ave}, gives the average value of the internal magnetic field for a given temperature. The values for the second moment evaluated from parameter a_6 were fit to the second moment model.

For our evaluation, the coherence length was fixed at a value of 0.03 k$\dot{A}$ and the critical temperature was fixed at a value of 90K. The penetration depth is allowed to vary within a range from 2.3 k$\dot{A}$ to 2.9 k$\dot{A}$. The displacements of type u_p have a linear relation with the penetration depth whereas the displacements of type u_l have an inverse relation with the penetration depth. When evaluating the BCS model, we choose nv in a range from 0.15 to 0.8. Our choice of nv negligibly affects the parameters of interest, u_p and u_l. There are no large discrepancies between models for the statistical measurement of the fit. We find that the displacements of type u_p dominate for the sample BSCCO which suggests a pancake-like nature. Fig. 13, 14, 15, and 16 show the experimental data compared to the theoretical fits. The theoretical fits are fairly similar for each theoretical model used. One reason for the statistical deviance in the 1 and 3 T fields is that those experimental data points have small error bars. These error bars are produced when the data was originally fit with function 34.

Table 1: Parameters from the vortex pinning model using the Empirical Model.

B (T)	$\lambda(0)$	E_{p0}	a (k$\dot{A}$)	u_{l0}/a	u_p/a	χ^2
1.0	2.9	73.1	0.489	0.0285	0.383	1.80
	2.7	70.4		0.0265	0.398	
	2.5	70.4		0.0231	0.413	
	2.3	70.3		0.0200	0.428	
2.7	2.9	113	0.297	0.0468	0.439	1.16
	2.7	113		0.0412	0.451	
	2.5	112		0.0360	0.464	
	2.3	112		0.0310	0.478	
3.0	2.9	75.0	0.282	0.0473	0.480	3.78
	2.7	75.0		0.0417	0.491	
	2.5	75.0		0.0364	0.503	
	2.3	75.0		0.0314	0.516	
6.0	2.9	65.0	0.199	0.0319	0.402	1.08
	2.7	65.0		0.0281	0.416	
	2.5	65.0		0.0245	0.430	
	2.3	65.0		0.0212	0.444	

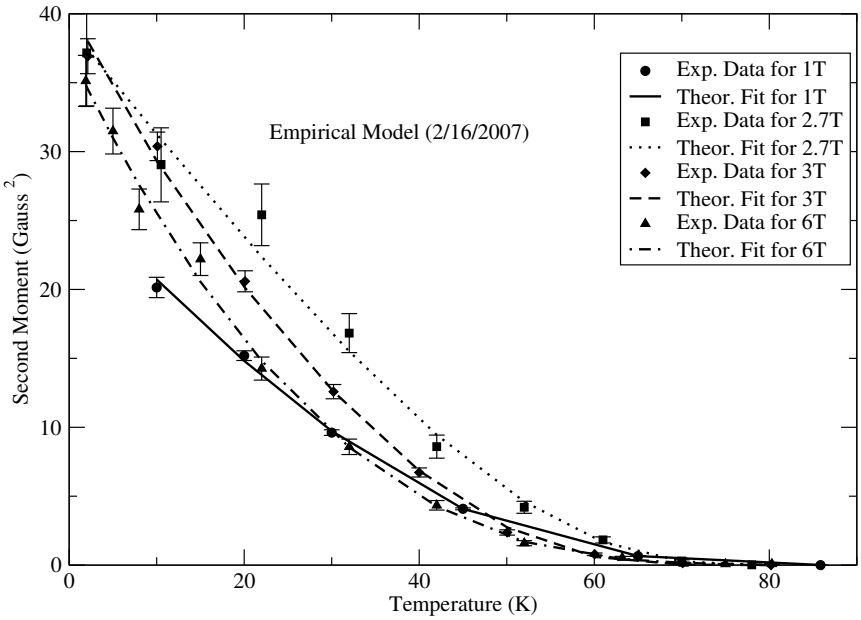

Figure 13: This figure shows the second moment of the magnetic field calculated from the parameters in function 34 for the four fields: 1T, 2.7T, 3T, and 6T. The theoretical fit for vortex pinning model proposed

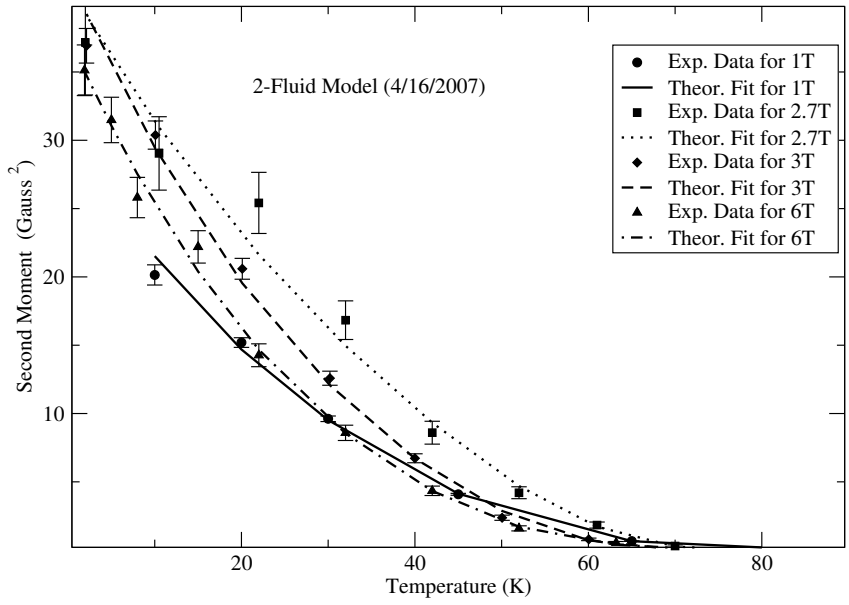

Figure 14: This figure shows the second moment of the magnetic field calculated from the parameters in function 34 for the four fields: 1T, 2.7T, 3T, and 6T. The theoretical fit for vortex pinning model proposed by E.H. Brandt is shown for the 2-Fluid model.

Table 2: Parameters from the vortex pinning model using the 2-Fluid Model.

B (T)	$\lambda(0)$	E_{p0}	a (k$\dot{A}$)	u_{l0}/a	u_p/a	χ^2
1.0	2.9	43.1	0.489	0.0417	0.426	4.28
	2.7	43.1		0.0369	0.438	
	2.5	43.1		0.0322	0.452	
	2.3	43.1		0.0279	0.466	
2.7	2.9	55.4	0.297	0.0549	0.501	1.60
	2.7	55.4		0.0483	0.512	
	2.5	55.4		0.0422	0.524	
	2.3	55.4		0.0364	0.536	
3.0	2.9	43.1	0.282	0.0560	0.529	4.46
	2.7	43.1		0.0493	0.567	
	2.5	43.1		0.0430	0.548	
	2.3	43.1		0.0372	0.559	
6.0	2.9	38.4	0.199	0.0519	0.477	1.08
	2.7	38.4		0.0455	0.521	
	2.5	38.4		0.0398	0.501	
	2.3	38.4		0.0344	0.514	

Table 3: ul/a and up/a; functional form bcs model (nv=0.15)

B (T)	$\lambda(0)$	E_{p0}	a (k$\dot{A}$)	u_{l0}/a	u_p/a	χ^2
1.0	2.9	58.4	0.489	0.0197	0.187	2.21
	2.7	58.4		0.0174	0.193	
	2.5	58.4		0.0152	0.201	
	2.3	58.3		0.0132	0.208	
2.7	2.9	106	0.297	0.0298	0.126	1.44
	2.7	106		0.0351	0.129	
	2.5	105		0.0306	0.133	
	2.3	105		0.0264	0.137	
3.0	2.9	64.1	0.282	0.0443	0.133	5.85
	2.7	64.1		0.0390	0.137	
	2.5	64.1		0.0341	0.141	
	2.3	64.1		0.0294	0.144	
6.0	2.9	50.0	0.199	0.0283	0.0801	1.14
	2.7	50.0		0.0249	0.0828	
	2.5	50.0		0.0217	0.0856	
	2.3	50.0		0.0188	0.0885	

Table 4: Parameters from the vortex pinning model using the BCS model with nv=0.2

B (T)	$\lambda(0)$	E_{p0}	a (k$\dot{A}$)	u_{l0}/a	u_p/a	χ^2
1.0	2.9	58.4	0.489	0.0197	0.187	2.21
	2.7	58.4		0.0174	0.193	
	2.5	58.3		0.0152	0.201	
	2.3	58.3		0.0132	0.208	
2.7	2.9	106	0.297	0.0398	0.126	1.44
	2.7	106		0.0351	0.129	
	2.5	105		0.0306	0.133	
	2.3	105		0.0264	0.137	
3.0	2.9	64.1	0.282	0.0443	0.134	5.85
	2.7	64.0		0.0391	0.137	
	2.5	64.0		0.0341	0.140	
	2.3	64.0		0.0294	0.144	
6.0	2.9	50.0	0.199	0.0283	0.0801	1.14
	2.7	50.0		0.0249	0.0828	
	2.5	50.0		0.0218	0.0856	
	2.3	50.0		0.0188	0.0885	

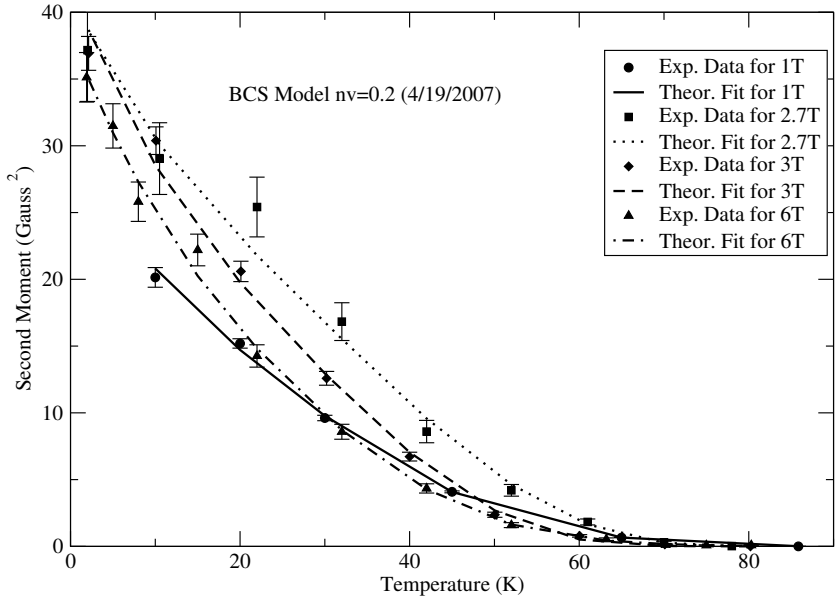

Figure 15: This figure shows the second moment of the magnetic field calculated from the parameters in function 34 for the four fields: 1T, 2.7T, 3T, and 6T. The theoretical fit for vortex pinning model proposed

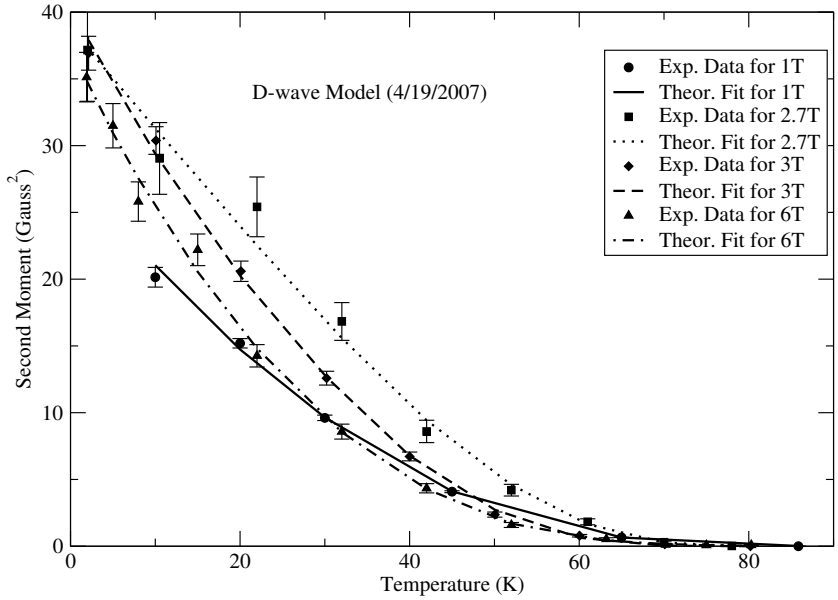

Figure 16: This figure shows the second moment of the magnetic field calculated from the parameters in function 34 for the four fields: 1T, 2.7T, 3T, and 6T. The theoretical fit for vortex pinning model proposed by E.H. Brandt is shown for the D-wave model.

Table 5: Parameters from the vortex pinning model using the BCS model with nv=0.25

B (T)	$\lambda(0)$	E_{p0}	a (k$\dot{A}$)	u_{l0}/a	u_p/a	χ^2
1.0	2.9	58.3	0.489	0.0198	0.187	2.21
	2.7	58.3		0.0174	0.193	
	2.5	58.3		0.0153	0.201	
	2.3	58.3		0.0132	0.208	
2.7	2.9	106	0.297	0.0398	0.126	1.44
	2.7	105		0.0351	0.129	
	2.5	105		0.0306	0.133	
	2.3	105		0.0264	0.137	
3.0	2.9	64.1	0.282	0.0443	0.134	5.85
	2.7	64.1		0.0390	0.137	
	2.5	64.1		0.0341	0.141	
	2.3	64.0		0.0294	0.144	
6.0	2.9	50.0	0.199	0.0283	0.0801	1.14
	2.7	50.0		0.0249	0.0828	
	2.5	50.0		0.0218	0.0856	
	2.3	50.0		0.0188	0.0885	

Table 6: Parameters from the vortex pinning model using the BCS model with nv=0.3

B (T)	$\lambda(0)$	E_{p0}	a (k$\dot{A}$)	u_{l0}/a	u_p/a	χ^2
1.0	2.9	58.2	0.489	0.0199	0.187	2.21
	2.7	58.1		0.0176	0.194	
	2.5	58.1		0.0154	0.201	
	2.3	58.1		0.0133	0.208	
2.7	2.9	105	0.297	0.0399	0.126	1.44
	2.7	105		0.0351	0.129	
	2.5	105		0.0306	0.133	
	2.3	105		0.0264	0.138	
3.0	2.9	64.0	0.282	0.0443	0.134	5.85
	2.7	64.0		0.0391	0.137	
	2.5	63.9		0.0341	0.141	
	2.3	63.9		0.0295	0.144	
6.0	2.9	49.9	0.199	0.0284	0.0801	1.14
	2.7	49.9		0.0250	0.0828	
	2.5	49.9		0.0218	0.0856	
	2.3	49.9		0.0188	0.0885	

Table 7: Parameters from the vortex pinning model using the BCS model with nv=0.6

B (T)	$\lambda(0)$	E_{p0}	a (k$\dot{A}$)	u_{l0}/a	u_p/a	χ^2
1.0	2.9	53.6	0.489	0.0238	0.189	2.52
	2.7	53.6		0.0210	0.196	
	2.5	53.6		0.0184	0.203	
	2.3	53.6		0.0159	0.210	
2.7	2.9	94.1	0.297	0.0414	0.127	1.51
	2.7	94.0		0.0365	0.131	
	2.5	93.9		0.0318	0.135	
	2.3	93.8		0.0275	0.139	
3.0	2.9	59.1	0.282	0.0462	0.136	5.70
	2.7	59.1		0.0407	0.139	
	2.5	59.1		0.0355	0.143	
	2.3	59.0		0.0307	0.146	
6.0	2.9	47.4	0.199	0.0312	0.0812	1.14
	2.7	47.4		0.0275	0.0839	
	2.5	47.4		0.0240	0.0866	
	2.3	47.4		0.0208	0.0895	

Table 8: Parameters from the vortex pinning model using the BCS model with nv=0.8

B (T)	$\lambda(0)$	E_{p0}	a (k$\dot{A}$)	u_{l0}/a	u_p/a	χ^2
1.0	2.9	52.7	0.489	0.0265	0.193	4.24
	2.7	52.7		0.0233	0.199	
	2.5	52.7		0.0204	0.206	
	2.3	52.7		0.0177	0.213	
2.7	2.9	80.6	0.297	0.0447	0.132	1.54
	2.7	80.5		0.0393	0.135	
	2.5	80.5		0.0343	0.139	
	2.3	80.4		0.0297	0.143	
3.0	2.9	53.6	0.282	0.0490	0.140	5.26
	2.7	53.6		0.0432	0.143	
	2.5	53.6		0.0377	0.146	
	2.3	53.5		0.0325	0.150	
6.0	2.9	45.1	0.199	0.0350	0.0830	1.12
	2.7	45.1		0.0308	0.0856	
	2.5	45.1		0.0269	0.0883	
	2.3	45.1		0.0233	0.0911	

Table 9: Parameters from the vortex pinning model using the D-wave model.

B (T)	$\lambda(0)$	E_{p0}	a (k$\dot{A}$)	u_{l0}/a	u_p/a	χ^2
1.0	2.9	86.2	0.489	0.0359	0.186	3.66
	2.7	86.2		0.0316	0.193	
	2.5	86.2		0.0276	0.200	
	2.3	86.1		0.0238	0.207	
2.7	2.9	111	0.297	0.0629	0.135	1.10
	2.7	111		0.0553	0.139	
	2.5	111		0.0483	0.143	
	2.3	111		0.0416	0.147	
3.0	2.9	79.9	0.282	0.0628	0.136	3.18
	2.7	79.9		0.0553	0.140	
	2.5	79.8		0.0482	0.143	
	2.3	79.8		0.0416	0.147	
6.0	2.9	74.1	0.199	0.0496	0.0774	1.01
	2.7	74.1		0.0437	0.0802	
	2.5	74.0		0.0381	0.0831	
	2.3	74.0		0.0329	0.0861	

4 Conclusion

We have used a back-to-back heterodyned Guassian-Gaussian to fit μ-SR data. These fits have been analyzed with a pinning model proposed by Brandt. We found that for BSSCO displacements of type u_p dominate which seems reasonable considering its pancake-like nature. We have found that the statistical difference is not large enough to differenitiate between the different models for the penetration depth. We cannot conclude decisively from vortex pinning whether the superconductor BSCCO is d-wave or s-wave.

References

[1] P.G. de Gennes. *Superconductivity of Metals and Alloys*. Addison-Wesley Publishing Company, 1966.

[2] Charles P. Poole, Jr., Horacio A. Farach, and Richard J. Freswick. *Superconductivity*. Academic Press, 1995.

[3] Orest G. Vendik, Irina B. Vendik, and Dimitri I. Kaparkov. Emperical model of the microwave properties of high-temperature superconductors. *IEEE Transactions on MIcrowave Theory and Techniques*, 46:469–478, 1998.

[4] D. Shoenberg. *Superconductivity*. Cambridge University Press, 1965.

[5] Michael Tinkham. *Introduction to Superconductivity*. McGraw-Hill, Inc, 1996.

[6] Anderson and Morel. *Phys. Rev.*, 123:1911, 1961.

[7] M. H. S. Amin, M. Franz, and Ian Affleck. Effective penetration depth in the vortex state of a d-wave superconductor. *Condensed Matter*, 3:1–4, 2000.

[8] D.R. Harshman, W.J. Kossler, X. Wan, A.T. Fiory, A.J. Greer, D.R. Noakes, C.E. Stronach, E. Koster, and John D. Dow. Nodeless pairing in single-crystal $YBa_2Cu_3O_7$. *Phys. Rev. B*, 69:174505, 2004.

[9] A.T. Fiory, D.R. Harshman, J. Jung, I.-Y. Isaac, W.J. Kossler, A.J. Greer, D.R. Noakes, C.E. Stronach, E. Koster, and John D. Dow. Fluxon pinning in the nodeless pairing state of superconducting $YBa_2Cu_3O_7$. *Electronic Materials*, 34:474–483, 2005.

[10] E.H. Brandt. Magnetic-field variance in layered superconductors. *Phys. Rev.*, 66:3213–3216, 1991.

[11] W. J. Kossler and A. J. Greer. trix06, 2001.

[12] A. Yaouanc, P. Dalmas de Reotier, and E.H. Brandt. *Phys. Rev. B*, 55:11107, 1997.

[13] E.H. Brandt. Thermal fluctuation of the vortex positions in high-T_c superconductors. *Physica C*, 162-164:1167–1168, 1989.

[14] H. Suhl. Inertial mass of a moving fluxoid. *Phys. Rev.*, 14:226–229, 1965.

[15] Neil W. Ashcroft and N. David Mermin. *Solid State Physics*. Saunders College, 1976.

[16] G. Blatter, M.V. Feigel'man, V.B. Geshkenbein, A.I. Larkin, and V.M. Vinokur. Vortices in high-temperature superconductors. *Reviews of Modern Physics*, 66:1125–1388, 1994.

[17] Pintu Sen, S.K. Bandyopadhyay, P.M.G. Nambissan, R. Ganguly, P. Barat, and P. Mukherjee. The study of inter and intragranular pinning behavior of oxygen irradiated textured polycrystalline $Bi_2Sr_2CaCu_2O_{8+\delta}$ and $Bi_{1.84}Pb_{0.34}Sr_{1.91}Ca_{2.03}Cu_{3.06}O_{10+}$*elta* superconductors. *Physica C: Superconductivity*, 407:55–61, 2004.

[18] C.S. Pande and M. Suenaga. A model of flux pinning by grain boundaries in type-II superconductors. *Applied Physics Letters*, 29:443–444, 1976.